

Global precipitation estimates from cross-track passive microwave observations using a physically-based retrieval scheme.

Chris Kidd^{1,2*}, Toshi Matsui^{1,2}, Jiundar Chern^{1,2}, Karen Mohr², Chris Kummerow³ and Dave Randel³,

¹*Earth System Science Interdisciplinary Center, University of Maryland, College Park, MD 20740*

²*NASA/Goddard Space Flight Center, Greenbelt, MD 20771.*

³*Colorado State University, Fort Collins, CO 80523*

*Corresponding author, (p) 301-614-6091, chris.kidd@nasa.gov

Abstract

The estimation of precipitation across the globe from satellite sensors provides a key resource in the observation and understanding of our climate system. Estimates from all pertinent satellite observations are critical in providing the necessary temporal sampling. However, consistency in these estimates from instruments with different frequencies and resolutions is critical. This paper details the physically-based retrieval scheme to estimate precipitation from cross-track (XT) passive microwave (PM) sensors onboard the constellation satellites of the Global Precipitation Measurement (GPM) mission. Here the Goddard PROFiling (GPROF) scheme, a physically-based Bayesian scheme developed for conically-scanning (CS) sensors, is adapted for use with XT-PM sensors. The present XT GPROF scheme utilizes a model-generated database to

overcome issues encountered with an observational database as used by the CS scheme. The model database ensures greater consistency across meteorological regimes and surface types by providing a more comprehensive set of precipitation profiles. The database is bias-corrected against the CS database to ensure consistency in the final product. Statistical comparisons over Western Europe and the United States show that the XT GPROF estimates are comparable with those from the CS scheme. Indeed, the XT estimates have higher correlations against surface radar data, while maintaining similar root mean squared errors (RMSE). Latitudinal profiles of precipitation show the XT estimates are generally comparable with the CS estimates although in the southern mid-latitudes the peak precipitation is shifted Equator-wards while over the Arctic large differences are seen between the XT and the CS retrievals.

1 Introduction

The estimation and mapping of precipitation across the Earth's surface is of great importance. Precipitation (rainfall and snowfall) is fundamental to many aspects of life on Earth, through the provision of fresh water that impacts our economic and social wellbeing. On a scientific level, precipitation plays a fundamental role in linking the Earth's water and energy cycles. To properly understand precipitation within the Earth System, it is necessary to quantify it on a global scale. While rain (and snow) gauges remain the *de facto* source of conventional information on precipitation their uneven distribution, and therefore their representativeness, limits their usefulness for measuring global precipitation. Similarly, surface radar datasets have limited spatial extent. The ability of satellite instrumentation to provide regular global observations is therefore a key component of any global precipitation measurement system.

Satellite observations using visible (Vis) and infrared (IR) images from low Earth orbiting (LEO) or geostationary (GEO) satellites provide regular observations of clouds from which estimates of precipitation may be generated. However, although precipitation originates from clouds not all clouds produce precipitation. More importantly, the relationship between the cloud top properties and the precipitation reaching the surface is indirect. Passive microwave (PM) radiometers allow a more direct measure of precipitation to be made since these frequencies are more sensitive to precipitation-sized particles. Multi-frequency PM instruments (e.g. the Special Sensor Microwave Imager Sounder, SSMIS, or the Microwave Humidity Sounder, MHS) allow more complex methods to be used to extract precipitation estimates over a range of different regimes. In 1997 the Tropical Rainfall Measuring Mission (TRMM) was launched, hosting a number of precipitation-related instruments, notably the TRMM Microwave Imager (TMI) and the Precipitation Radar (PR); TRMM finally ended data collection on 8 April 2015. Building upon the success of TRMM, the Global Precipitation Measurement mission (GPM) Core Observatory was launched in 2014, joining a constellation of international satellites equipped with precipitation-capable sensors and providing improved capabilities for the measurement of precipitation from passive and active microwave sensors (Hou et al. 2014).

Alongside the technological development of satellite instrumentation, techniques have been developed and evolved to extract information on precipitation from the satellite observations. Although the Vis/IR observations are relatively indirect, their frequent temporal availability from GEO sensors permits the timely production of near real-time products for applications such as flood forecasting. The more direct observations made by PM sensors have led to a range of precipitation estimates using empirical and/or physically-based schemes. Empirical techniques built upon basic radiometric properties of precipitation, such as the Polarization-Corrected

Temperature (Spencer et al. 1986; Kidd 1998) and Scattering Index (Ferraro et al. 1998), have achieved a degree of success (see Kidd et al. 1998). However, while empirically-based schemes are generally simpler and computationally faster, physically-based schemes generally provide more information on precipitation, such as types of hydrometeor and even atmospheric profiles of precipitation. The Goddard PROFiling (GPROF) scheme (Kummerow et al, 2001, 2015) is an example of the latter and has been developed for use with multi-channel microwave observations from conically-scanning (CS) radiometers such as the Special Sensor Microwave/Imager (SSM/I) and the TRMM Microwave Imager (TMI). In the GPM era the constellation of precipitation-capable sensors includes both CS and cross-track (XT) sensors necessitating the incorporation of XT observations into the GPROF scheme.

This paper describes the adaptation of the GPROF scheme to utilize observations from the XT PM instruments. Section 2 describes the GPROF scheme in detail together with the steps required to adapt it to the observations from the XT sensors, and in particular the incorporation of model information, which is described in Section 3. Initial results from testing of the new GPROF XT scheme using data from the MHS are provided in Section 4, while Section 5 provides a discussion of the results and future directions.

2 The GPROF retrieval scheme

Although the presence of precipitation is often evident in maps of PM brightness temperatures, providing unambiguous retrievals of precipitation is often difficult. This is primarily due to the variability of the surface background, and/or the non-unique observed spectral signatures to hydrometeor profiles/surface rainfall relationships. A greater insight into the radiometric

signature may be obtained through inverse radiative transfer modelling, although such techniques are ultimately limited by the model itself and the computational requirements.

One of the better-known physically-based precipitation retrieval techniques is the GPROF scheme, originally conceived by Kummerow and Giglio (1994). The scheme was devised to not only provide an estimate of the surface precipitation, but also an estimate latent heat release (amongst other parameters) from the vertical structure of the precipitation. In its purest form, the observed brightness temperatures (Tbs) are processed through inverse radiative transfer modelling to provide an estimate of precipitation (see Kummerow et al. 1996; Olson et al. 2007). However, due to the computational expense of such a scheme a Cloud Radiation Model (CRM) - based *a priori* database is employed to provide fully parametric precipitation estimates through a conditional probalistic Bayesian retrieval scheme; critically, once the *a priori* CRM-based database had been established for one sensor, it can be extended to include other passive microwave sensors.

The basic assumption of the scheme is that the CRM database can accurately describe and represent the precipitation to be retrieved. Early CRM simulations (see Tripoli, 1992; Tao and Simpson, 1993) had relatively simple microphysical schemes that limited not only the representativeness and accuracy of the results, but also proved to be computationally expensive. Similarly, the matching of the satellite observations to the CRM database was (at the time) time-consuming, consequently a rain/no-rain screen was introduced in the earlier versions of GPROF so that the database was only accessed for observations likely to have rain. The CRM database was then interrogated to find a profile that best matches the spectral signature of the satellite

observation. However, no distinct precipitation signatures may exist since the observed radiances are affected by a range of factors other than precipitation, including surface effects, radiometric noise, together with beam filling effects resulting from the (relatively) large footprints, etc. Furthermore, since PM sensors have a limited number of channels and thus cannot uniquely identify all the possible radiometric signatures, the accuracy of the retrieval is based upon the ability of the observations to resolve the true spectral signature (Smith et al. 1994). While it is possible to select the database entry with the closest signature, the retrieved value can only be an approximation of the true value. A Bayesian scheme is therefore used to generate not only an estimate of precipitation, but also an estimate of uncertainty of the retrieval itself (see Elsaesser and Kummerow 2015).

The GPROF retrieval scheme has undergone a number of modifications over time to improve the retrievals, including improvements to the radiative transfer model used in the generation of the *a priori* database, freezing level heights over the oceans, discrimination of regions of stratiform vs convective precipitation, cold surface screening, etc. (see Kummerow et al. 2001). The current GPROF scheme implemented for the CS radiometer observations, known as GPROF2014, is described in Kummerow et al. (2015). To better define the range of suitable hydrometeor profiles in the *a priori* database, together with improving the computational efficiency the current CS-GPROF scheme, the database incorporates model-derived measures of skin temperature (T_s) and total precipitable water (TPW). The categorization of the profiles by T_s and TPW is based upon the findings of Berg et al. (2006) to account for regional differences in the relationship between surface precipitation and satellite radiances. Furthermore, since the background surfaces are deemed to be influential on the spectral signature of the observed T_b s, separate databases are

generated for 15 different surface types, including land, ocean, ice, etc. The profiles included in each of these databases are based upon the satellite observed radiances with rain rates derived from co-located surface-based radar or satellite-based radar (i.e. CloudSat Cloud Profiling Radar, CPR, and/or the TRMM Precipitation Radar, PR). In the retrieval process, model-generated Ts, TPW and surface type are attached to each set of observed brightness temperatures: the surface type selects the appropriate database and the Ts and TPW identifies which set of profiles within the database to use for the retrieval.

Thus, the GPROF scheme comprises of three main processing steps as identified in Figure 1. The first involves the generation of the *a priori* database that contains radiances with associated surface rainfall, hydrometeor profiles and other pertinent data. The second step preprocesses the satellite observations by attaching the surface types and model-derived Ts and TPW to the set of brightness temperatures for each satellite footprint. The final stage performs the Bayesian retrieval of the precipitation by comparing the satellite observations to the radiances in the appropriate database with the same Ts and TPW.

2.1 Adaption of GPROF to the XT sensors

The inclusion of the XT sensors within the GPROF scheme is of great importance; first, it doubles the number of current PM sensors available for precipitation estimation and second, it provides a consistent approach to the retrieval of precipitation from the passive microwave radiometers that are part of the GPM constellation (see Table 1). The main differences between the CS and XT instruments are primarily the scanning geometry and channel selection. CS radiometers provide a (nearly) constant Earth Incidence Angle (EIA) and therefore consistent

footprint resolution (at each frequency) and polarization across the swath of the sensor. However, XT instruments scan perpendicular to the satellite's trajectory such that the center of scan is close to, or at the sub-satellite point. Observations are taken at equal scan angles across the satellite swath resulting in a changing EIA with each scan position and consequently the size of each footprint increases away from the nadir point, together with changes in the polarization and the length of the atmospheric path between the Earth's surface to the sensor. In addition, CS radiometers have traditionally used (imaging) channel frequencies typically between about 6.9 and 90 GHz, while XT sensors have utilized higher (sounding) frequencies up to about 190 GHz. However, newer CS instruments including the Special Sensor Microwave Imager Sounder (SSMIS) and the GPM Microwave Imager (GMI) also incorporate these higher frequencies.

Although most precipitation retrieval schemes have concentrated the observations from CS instruments (see Kidd and Huffman 2011; Kidd and Levizzani 2011), a number of techniques have been developed to exploit the observations from XT sensors. These include neural network approaches by Surussavadee and Staelin (2008) and Sano et al. (2015), the 183-WSL technique of Laviola et al. (2013) and a technique using canonical analysis by Casella et al. (2015). Of particular interest in the context of this paper is the Microwave Integrated Retrieval System (MiRS, Iturbide-Sanchez et al. 2011; Boukabara et al. 2011) that is used to generate a number of geophysical parameters from both CS and XT passive microwave observations using an iterative physical inversion scheme, although only the NOAA-18 and MetOp-A XT MHS sensors are used for precipitation estimation. However, current schemes only provide XT-only or CS-only retrievals of precipitation. The GPROF scheme described in this paper is adapted so that the

retrievals from both the CS and XT sensors can be obtained through the same methodological framework.

The development of the XT-GPROF scheme has been based upon the MHS instrument, but recently extended to other XT sensors. The MHS has XT scan angles that vary from $+49.44^\circ$ to -49.44° resulting in an EIA ranging from -58° to $+58^\circ$ and resolutions varying from 15.88×15.88 km at nadir to 27.10×52.83 km at the swath edge (along-track \times cross-track). In addition, the polarization changes from primarily vertical to primarily horizontal (or vice versa depending on the channel), and the atmospheric path increases to 1.88x that of the nadir path at swath edge. Although the details for each XT sensor are similar, they have subtle differences due to scan angles, frequencies used and nominal sensor resolution. The consequences of the variable EIA were therefore explored in the prototype XT GPROF scheme and are outlined below.

2.2 Prototype XT-GPROF scheme

In preparation for the operational version of the XT-GPROF scheme a prototype scheme was devised and tested; this prototype version augmented the CS-GPROF scheme with features that were deemed to be useful for the XT-GPROF version. As noted above, the changing EIA of the XT sensors impacts the resolution, polarization and atmospheric path of the observations. It was therefore assumed that observations at each scan position would need to be considered separately, or at least in groups of alike scan positions. An initial comparison of the impact of polarization with scan position upon the retrievals revealed only small differences, consequently the variation in the polarization with scan position was not considered at this stage. The effect of the resolution of the observations was also investigated. Rather than provide databases for each

of the 90 scan positions, databases were generated for 5 similar EIA scan position bins. Since the CS-GPROF scheme already comprises of 15 databases (one for each surface type), this meant that the prototype XT scheme required a total of 75 databases (15 surfaces x 5 scan position bins).

The databases generated for the prototype version of the scheme were generated from matchups between the MHS satellite observations matched with collocated surface or satellite radar measurements, similar to that of the CS-GPROF scheme. Although this methodology worked well for the CS-GPROF databases, the number of available MHS-surface/satellite radar matchups was more limited for the XT databases. In addition, a greater number of databases (due to incorporating scan-positions) reduces the sample-size in each database resulting in increased noise and potentially missing retrievals. Since the MHS-channel frequencies are less sensitive to the surface background it was decided produce a single, surface-blind database that relied solely upon the modeled Tbs to adequately resolve the precipitation over any surface and for any scan position. Furthermore, to ensure an adequate number of database entries, the database was populated with profiles from the Multi-scale Modeling Frameworks (MMF) v2.1 model (as described in section 3).

2.3 The XT-GPROF scheme

The characteristics of the current operational XT-GPROF scheme, together with those of the CS-GPROF scheme, are summarized in Table 2. The key difference between the two schemes is that the XT version uses a single model-derived database as opposed to the observation-derived databases of the CS-version. To ensure consistency between the CS and XT databases the mean

rainrate per XT database bin is bias-corrected against the CS databases to ensure comparable retrievals. In addition, the XT scheme incorporates a simple empirically-derived scan position adjustment that mitigates the effects of the changing resolution and beam filling upon the precipitation retrievals. This correction is designed to ensure that the precipitation retrieved at all scan angles is comparable with the nadir-only calculations from the MMF model. Also of note, unlike the diagnostic identification of frozen precipitation (i.e. snow) in the CS-GPROF scheme, falling snow is quantified directly from the XT retrieval itself.

Crucial to the success of the XT-GPROF retrieval scheme is the MMF model. The primary purpose of using the MMF-simulated database is to establish a quality-controlled and physically-based precipitation retrieval algorithm consistent with the GPM core satellite as well as the GPM constellation satellites. The advantage of using a MMF-simulated database includes i) the simulated microwave Tbs are derived from the identical physical assumptions and calculation methods; ii) it is straightforward to generate a Tb database for all constellation satellite sensors, iii) the database quality can be readily tracked for further improvement, and iv) the database can include drizzle and snowfall signals that might be missed through the use of an observation-derived database. Critically the MMF provides physically consistent surface and environmental parameters together with associated radiances necessary to generate the XT database.

3 The MMF model-derived database

3.1 The MMF model

The NASA MMF model is composed of the Goddard Earth Observatory System V4 (GEOS4) and the Goddard Cumulus Ensemble (GCE) model. The GCE utilizes the new Goddard 4ICE microphysics, which includes explicit hail categories and many improved microphysics parameterizations (Lang et al. 2014, Chern et al. 2015). GEOS4 simulates general circulations and surface flux with a climate-scale grid configuration ($2.5^{\circ} \times 2.0^{\circ}$ horizontal grid spacing), which forces fine-resolution two-dimensional GCE models with a cloud-resolving-scale grid configuration (4 km horizontal grid spacing). The GCE explicitly simulates cloud dynamics and microphysics processes every 10 seconds, and the mean profiles of the GCE meteorological fields and hydrometeors feed back to the GEOS4 grid every hour. For computational efficiency, the GCE is configured in a two-dimensional (2D) grid (64×1 horizontal and 41 vertical) using a cycling boundary condition. In this way, numerous copies of explicit cloud-resolving model simulations replace ill-posed parameterization of sub-grid convection and cloud processes in GEOS4. This hybrid structure of the climate model enables a more realistic representation of convection without using ill-posed convective parameterization, improving many cloud-related features, such as the diurnal cycle of precipitation (Tao et al. 2009), land-atmosphere interactions (Mohr et al. 2012), and distributions of ice water content (Chern et al. 2015).

Another advantage of using the MMF is that the spatial scale of MMF-simulated cloud-precipitation parameters is close to those of satellite observations. While a traditional climate model often assumes complex sub-grid distributions or overlapping patterns for evaluation against satellite data (Webb et al. 2001), the MMF explicitly simulates the physical structure of cloud and convective processes through the 2D GCE; thus, the satellite instrumental simulator can be applied straightforwardly. The precipitation and microphysics parameters of the MMF

simulations can be evaluated directly against the satellite measurements (Matsui et al. 2009); if these synthetic satellite observations are in reasonable agreement with specific satellite measurements, a set of MMF-simulated satellite signatures and geophysical parameters may be used to populate databases for similar satellite sensors (Matsui et al. 2013).

The drawback of using a MMF-simulated database is associated with the intrinsic nature of biases within models, including i) MMF dynamics and microphysics process and ii) forward model assumptions. These problems, especially the MMF biases, have been significantly reduced through various observation and model improvements, and are briefly summarized below:

- *Microphysics.* A new Goddard 4ICE microphysics scheme replaced the original Goddard 3ICE microphysics (Lang et al. 2014, Chern et al. 2015). This new scheme predicts an explicit hail category in addition to existing hydrometeor categories (cloud, rain, ice crystals, snow aggregate, and graupel). The occurrence of hail in convective cores is relatively rare and its spatial coverage is also very small (less than a few percent), but it improves the representation of strong precipitation intensity and the strong depression of microwave Tbs associated with convective core structure.
- *Vertical levels.* The original GCE vertical resolution contained 28 levels up to the tropopause. However, it was found that Rayleigh dampening in the upper model layers tends to suppress vertical velocity of deep convection (maxima: $\sim 10 \text{ m s}^{-1}$). Thus, the number of vertical levels were increased to 41 so that deep convection could be allowed to overshoot the tropopause, unaffected by Rayleigh dampening. As a result the maximum vertical velocity has been increased significantly (maxima $\sim 30 \text{ m s}^{-1}$), improving the representation of echo-top height distributions.

- *Background meteorology.* The free-running mode of long-term MMF (and any climate model) simulations often causes internal climate drift due to biases in the physics schemes and their interactions. For the production of the database, the background meteorology should be as close as possible to the observation. Consequently, the mean meteorological fields of the MMF simulation were nudged using the European Centre for Medium Range Weather Forecasts (ECMWF) Interim re-analysis (ERA-Interim) reanalysis. This suppresses the overestimation of high precipitation in the tropical warm pool region which are associated with frequent shallow convection in previous MMF simulations (Tao et al. 2009).

3.2 The RT model

The forward model used in the database generation is the GPM simulator suite of the Goddard Satellite Data Simulator Unit (G-SDSU, Matsui et al. 2013). Microwave brightness temperatures (T_b) are computed through a two-stream model with Eddington's Second Approximation (Kummerow 1993) along satellite FOV-slant paths (Olson et al. 2001). Land-surface emissivity is estimated from the satellite-estimated climatology map (Aires et al. 2011), while water-surface emissivity is based on an empirical parameterization as a function of salinity, wind speed, and temperature (Wilheit 1979). Note that surface emissivity and skin temperature are assumed homogeneous in the forward model and for each copy of the 2D GCE. Gaussian weighting functions of brightness temperatures are then used to generate the satellite-resolution T_b s in combination of specific beam widths of sensors, sensor viewing angle, satellite altitude, and local elevation.

Hydrometeor single-scattering properties are computed at each GCE grid cell via the Lorenz-Mie method with effective refractive indices through the Maxwell-Garnett mixture method. Single-scattering calculation follows the exact assumptions of Goddard 4ICE microphysics for size distributions and bulk effective density, including new empirical snow-graupel size and density mapping (Lang et al. 2014). Single-scattering properties are integrated over the two liquid and four ice categories to represent bulk single-scattering properties.

3.3 Implementation

The XT-GPROF scheme therefore currently relies on a single database (covering all surface types) which is derived from the MMF model. The MMF simulations were generated for 1 year from 1 January 2007 to 31 December 2007 with profiles sampled over the globe equidistantly every c. 200 km; large-scale meteorological conditions (temperature and humidity profiles) were nudged using the ERA-Interim every 24 h in order to avoid internal climate drift.

As noted above, to ensure consistency between the CS and XT retrievals the XT database is bias-corrected against the CS database. Figure 2 depicts the mean rain rate per database bin for the aggregated GMI databases and the MMF-derived database for the MHS sensor. While the general form of the databases are broadly similar, it can be seen that the MMF-derived database provides profiles over a greater range of T_s and TPW than the GMI database; the MMF-derived database ranges from 189-344 K for T_s and 0-95 g Kg⁻¹ for TPW compared with the GMI database ranging from 230-337 K for T_s and 0-80 g Kg⁻¹ for TPW. While both schemes use T_s and TPW derived from the ECMWF model, the key difference is the restriction imposed by sampling on the GMI observational database. One of the consequences of the CS database being

based upon observations is that the retrieval will fail if it attempts to retrieve a profile beyond any previously seen meteorological condition. While the distribution of the mean rain rates is similar between the two databases, the greater range of the MMF database provides higher rain rate profile entries for high values of TPW.

The MMF-derived databases initially developed to generate products from the MHS sensor (Kidd 2014a-d) are currently being extended to include the Advanced Technology Microwave Sounder (ATMS) on the US Suomi National Polar-orbiting Partnership (NPP) satellite and the Sondeur Atmosphérique du Profil d'Humidité Intertropicale par Radiométrie (SAPHIR) on the French/Indian Megha-Tropiques satellite.

4. Verification and validation

The XT-GPROF retrievals are generated in near real time by the GPM Precipitation Processing System (PPS) at NASA's Goddard Space Flight Center. The XT v1-2 retrievals (Kidd 2014a-d) for the MHS and CS v1-4 retrievals (Kummerow 2014a-e) for the AMSR2, GMI and SSMIS are used in this study. The spatial resolution of the CS-GPROF retrievals are set by the size of the size of each sensor's 3 dBZ sensitivity at 37 GHz; this equates to a retrieval resolution of 12×7 km for AMSR2, 14×8.6 km for GMI and 44.2×27.5 km for SSMIS. The scan position corrected XT retrievals are deemed to be comparable with the nadir-only 15.88×15.88 km resolution of the model-generated database, regardless of scan position. In addition, comparisons were also made for the SSMIS using a resolution of 15×15 km to permit more consistent comparisons with those from the other sensors.

Surface radar data over two regions, the United States, and Western Europe, was used as ground ‘truth’; both these regions have extensive, high-quality radar coverage suitable for the validation of satellite products (see Kidd et al. 2012; Ebert et al. 2007). However, due the spatial and temporal sampling of the radar data over these regions two different approaches were adopted for the satellite/surface comparison. Over the United States radar data is available at a spatial resolution of $0.01^{\circ} \times 0.01^{\circ}$ every 2 minutes from the National Oceanic and Atmospheric Administration (NOAA) National Severe Storms Laboratory (NSSL) Multi-Radar/Multi-Sensor (MRMS) system (Kirstetter et al. 2012). The satellite estimates were subsetting from the orbital files for each two minute segment; the time stamp was set to the end time to match the timestamp of the corresponding radar data. The satellite footprints were then mapped to the radar data grid for each two minute segment and the radar data averaged within the satellite footprint to provide a corresponding surface rainfall value. For this comparison, only radar data with the highest quality index (see Kirstetter et al. 2012) equal to 1.0 over the entire footprint were included in the analysis. Furthermore, data west of 100°W were excluded in the analysis due to the paucity of radar coverage over the mountainous western United States.

Radar data over Western Europe (Met Office 2003) was obtained from the Centre for Environmental Data Archive (CEDA). The data are a composite of radars covering the United Kingdom, France, Germany and the Netherlands, mapped to an equal area projection at 5×5 km spatial resolution every 15 minutes. Due to the coarser resolution of the radar data, matching the surface radar to satellite footprints necessitates a different matching approach. The centers of each satellite footprint were mapped to the 5×5 km radar data; where the radar data was fully

within the satellite footprint a weight of 1.0 was assigned, otherwise a weight less than one was assigned on the margins of the satellite footprint based upon the fraction coverage of the satellite footprint. Since no radar quality index was available for the European radar data, a skill-score map derived from previous satellite/radar comparison (see Kidd and Hou 2012) was used to provide a measure of quality.

Precipitation retrieval by intensity:

One of the artifacts associated with the Bayesian retrieval scheme is that if any profile within the searched set of profiles within the database contains any precipitation, all retrievals using that bin will return a non-zero precipitation result leading to an exaggerated occurrence of precipitation. Figure 3 shows the satellite/surface-radar ratio of the accumulated (liquid-only) precipitation in 0.01 mm h⁻¹ bins for 6 March 2014 to 5 March 2015 over the US. The retrievals from all the sensors exhibit significant over estimation at low rainfall intensities: in particular, the AMSR2 retrievals show nearly a 50-fold overestimation of precipitation accumulation in the lowest (>0.00-0.01 mm h⁻¹) bin, while the MHS show a more modest 8-fold overestimation. However, it should be noted that these very low-intensity comparisons are somewhat dubious due to the statistical nature of the retrieval and the sensitivity of the surface radar dataset to very light precipitation. Nevertheless, Figure 3 shows that the overestimation of light precipitation is matched by an underestimation of the moderate intensities for the AMSR2, GMI and MHS retrievals; the SSMIS underestimates the precipitation accumulation (about x0.7) across all intensities above 0.25 mm h⁻¹. Although some of this underestimation by the SSMIS could be attributed to the large retrieval footprint (44.2 x 27.5 km), it would be expected that this would be compensated by overestimation at other rain intensities.

Since all the retrievals overestimate the very light precipitation, it is therefore advisable to threshold the rain/no-rain boundary at about 0.1 mm h^{-1} , although differences occur in the threshold between the sensors and over different regions. The ideal rain/no-rain threshold may be found by adjusting the rain rate threshold of the satellite retrieval so that the rain and no-rain occurrences match those of the surface radar; Figure 4 maps these thresholds over the US for the retrievals from each of the four sensors. The SSMIS generally exhibits the lowest rain/no-rain thresholds generally below 0.2 mm h^{-1} , while the MHS shows the highest rain/no-rain threshold at about 0.2 mm h^{-1} over land, but higher over the coastal oceans; these higher thresholds indicate that the satellite estimates are overestimating the occurrence of precipitation in these regions. However, all show similar patterns in the distribution of the threshold, with generally higher values over the Mississippi valley, and lower values over the mountainous Western US, and along the Appalachians in the East. The variations in the distribution of the thresholds suggest a regional effect on the surface reference data (under/over estimation by the surface radar) or a surface background effect.

Statistical performance

Two basic statistical measures were used to assess the performance of the retrievals over Western Europe and the US, namely the correlation coefficient and root mean squared error (RMSE). The comparisons were performed on instantaneous retrievals using only high-quality radar data for each day between 6 March 2014 and 5 March 2015. A rain/no-rain threshold of 0.1 mm h^{-1} was set for both the satellite retrievals and the radar estimates (values less than 0.1 mm h^{-1} being set to zero). In addition, for the summary of daily statistical performance, only days on

which more than 1% of the radar data was raining were included in the analysis. Figure 5 shows the occurrence of the number of days which attained correlations within the respective correlation bins. At the native retrieval resolutions the SSMIS (44.2×27.5 km) performs best with more than 80% of the days having correlations of 0.6 and above; the MHS in comparison has about 45% of the days with correlations above 0.6. However, the large footprint of the SSMIS (based upon the resolution of the 37 GHz frequency channel) means that precipitation features are smoothed compared with retrievals with a higher-spatial resolution; consequently the correlations will be higher for the same precipitation events. If the SSMIS retrievals are compared with collocated radar sampled at 15×15 km (comparable with the other retrievals), the occurrence of correlations above 0.6 drops to less than 20%, less than those of the AMSR2, GMI or MHS. Performance of the retrievals for the RMSE shows a similar grouping: the higher resolution retrievals show a broad peak from about 0.4-0.6 to 1.2-1.4 mm h^{-1} , while the SSMIS has a more distinctive peak at 0.6-0.8 mm h^{-1} . However, if the SSMIS is compared at the higher resolution, the distribution of RMSE is similar to the other retrievals although with a higher occurrence in the lowest, 0.0-0.2 mm h^{-1} bin.

Over Western Europe the distribution of daily correlations has a greater range; over the US the correlations were concentrated between 0.3 and 0.8, over Europe correlations lie generally between 0.0 and 0.8, as shown in Figure 6. It can be seen that the performance of all the retrievals is relatively consistent with the MHS retrievals performing slightly better as noted by the higher occurrence of correlations in the 0.6-0.7 category. Interestingly, despite the larger footprint of the SSMIS, the retrievals are not significantly better than the higher-resolution retrievals (as was the case of the United States), and that the correlations are broadly similar

when the higher-resolution SSMIS retrievals are considered. Analysis of the RMSE scores show a similar performance between the different retrievals at the finer resolutions with peak RMSEs between 0.2-0.4 and 0.4-0.6 mm h⁻¹; the coarser native-resolution SSMIS retrieval having slightly lower (better) RMSE. The differences in statistical performance between the US and Europe are most likely a combination of different climate regimes and the relative quality of surface radar data.

The effectiveness of the XT scan-position correction on the retrieved precipitation is assessed through a comparison over the US between the edge-of-scan and near-nadir estimates. Scan positions 1-22 and 69-90 were assigned as edge-of-scan, while 23-68 as near-nadir. As Figure 7 shows, the differences in the correlation coefficient between these retrieval groups is small, with the edge-of-scan retrievals providing slightly better correlations than those near-nadir. We can therefore assume that the retrievals have comparable validity irrespective of scan position.

To assess the spatial variability of the correlation between the satellite and surface estimates, correlations were calculated between all instantaneous satellite/surface collocated matchups on a 1° × 1° grid for the period 6 March 2014 through 5 March 2015 over the US. The maps of the these correlations are plotted in Figure 8 for the four satellite products at their native retrieval resolution, together with those of the SSMIS at 15 × 15 km resolution. The paucity of radar coverage over the western half of the US is clearly visible with correlations typically less than 0.50. Over the eastern half of the US correlations are generally better than 0.60, with the SSMIS producing correlations over 0.70. However, if the SSMIS retrievals are compared at the 15 × 15

km resolution, these correlations drop to between about 0.60 and 0.65, similar to those of the other products.

Annual global estimates

Despite the comparable statistics performance of the XT retrievals with those of the CS over the US and Western Europe, a key issue is whether these estimates provide reasonable global estimates. The mean annual precipitation for all four sensor types has been calculated (for all data $\geq 0.0 \text{ mm h}^{-1}$) for the period 6 March 2014 through 5 March 2015 (the first year of GMI data availability) with the results shown in Figure 9. The CS retrievals produce similar estimates with all the main regional-scale features evident; the XT retrievals also show these features although subtle differences exist. The XT retrievals along the Inter-Tropical Convergence Zone (ITCZ) are generally slightly less than those of the CS retrievals with some regional variations, such as off the West coast of Africa. Precipitation in the mid-latitudes is broadly similar, although differences can be noted along the South Pacific convergence zone and along the storm tracks of the Southern Oceans. The AMSR2 and SSMIS estimates produce significant precipitation over the polar regions (the GMI only observes up to 68° N/S) with retrievals from the SSMIS producing mean daily precipitation of 3 mm d^{-1} (water equivalent), while the AMSR2 retrievals produce nearly 2 mm d^{-1} . Breaking the annual totals down into the occurrence of precipitation by intensity (see Figure 10) shows that the high latitudes exhibit the greatest differences between the retrievals with the MHS showing the least occurrence of precipitation over land and ocean across all intensities, although note the limited extent of the GMI data. At the mid-latitudes ($60^\circ\text{-}30^\circ\text{S}$ and $30^\circ\text{-}60^\circ\text{N}$) all the techniques have similar occurrences of precipitation intensity for land and for ocean, although the GMI generates more high-intensity

precipitation. Within the Tropics (30°S - 30°N) there appears to be more variation between the techniques and background surfaces: over the ocean the GMI and AMSR2 produce less light precipitation than the SSMIS and MHS retrievals, while over land the retrievals are similar for light precipitation. However, for higher rain intensities the GMI and AMSR2 have a higher occurrence of precipitation than the SSMIS and MHS retrievals.

Latitudinal profiles of mean daily rainfall are shown in Figure 11; the differences between the XT MHS retrievals and those of the CS retrievals are evident, particularly above 70°N and south of 30°S . Further analysis shows that above 70°N the CS retrievals are affected by melting snow and ice at the surface during the Arctic summer. South of 20°S , the XT retrievals show a peak in precipitation at about 35°S , north of that suggested by the CS retrievals. However, at higher southern latitudes the XT estimates are closer to those from the GPM Dual-frequency Precipitation Radar (DPR) than the CS estimates. Outside these regions the agreement is generally good, although the peak precipitation produced by the MHS at about 5°N is about 10% less than that of the CS sensors, but similar to that obtained by the DPR.

5. Discussion and Conclusion

Although the basic premise of the GPROF retrieval scheme is relatively simple, the implementation of the scheme is less straight forward, particularly so with the XT sensors. Overall the XT scheme aims to provide retrievals that are comparable with those of the CS retrievals to ensure a homogenous dataset, however fundamental differences between the sensor types necessitates variations in the retrieval scheme. The most notable differences between the

current schemes relate to the database itself. The choice of the MMF-modeled database rather than the observational database of the CS is primarily due to the representativeness of the database entries: Preliminary tests using a XT observational database produced too many ‘missing’ retrievals. In addition, the use of different data sources to generate an observational database potentially contributes additional noise within the database itself as well as potential inconsistencies between the different regimes used in the database creation. While the model itself is not perfect, one advantage of the modelled database is the consistency across the different profile entries: an increase in TPW or Ts leads to a corresponding and predictable change in the profile entry.

Statistical comparisons between the satellite retrievals and the surface radar data show that the model-based XT MHS retrievals are at least comparable with those of the observational-based CS retrievals. While the SSMIS retrievals outperform other estimates at its native retrieval resolution, the statistical performance of the SSMIS retrievals is much reduced when compared at a similar scale to the other retrievals. For similar spatial resolutions, the MHS retrievals exhibit generally higher correlations than the CS retrievals. Despite the MHS retrievals performing well statistically, some issues remain. As noted in Figures 3 and 4, the rain/no-threshold for the MHS retrievals is higher than those for the CS retrievals, particularly so over the coastal-ocean region.

In terms of the global distribution of mean annual precipitation (Figure 9) two principle regions can be identified where substantial differences occur between the XT and CS retrievals. The first is over the high latitude regions in the northern hemisphere where the CS retrievals (AMSR2 and

SSMIS) produce much more precipitation (c. 1.8 and c. 2.9 mm d⁻¹ respectively) than the XT MHS retrieval (0.2 mm d⁻¹). Although the MHS value appears low, the MHS results presented here are similar to the 2009-11 climatology provided by the MiRSv4.0 product in Boukabara et al. (2011); the AMSR2 and SSMIS values are certainly too high. Closer analysis of the data found that the majority of the precipitation generated by the AMSR2 and SSMIS retrievals was associated with the summertime melting of the snow and sea ice over the Arctic. The second region where discrepancies between the XT and CS retrievals are evident over the southern oceans, and in particular over the South Pacific Ocean around 30°S between 150°W and 120°W; here the MHS produces a maxima in the order of about 8 mm d⁻¹ whereas the CS retrievals show a less clearly defined maxima of about 6 mm d⁻¹ to the northwest. These differences are also evident in the latitudinal profiles shown in Figure 11, which also highlights the widespread differences between the XT and CS estimates over the southern hemisphere south of 30°S. If the estimates from the DPR are included it can be seen that although the MHS retrievals are too high around 35°S, the CS estimates are between 2 and 4 times that of the DPR or MHS estimates by 60°S. These differences require further investigation but probably arise from a combination of physical reasons and retrieval assumptions. For example, over the oceans the XT and CS use different combinations of channel frequencies, the XT using channel frequencies above 89 GHz while the CS sensors use primarily frequencies below 89 GHz, therefore the fundamental observation-rainfall relationships will be different. In addition, the observational database used by the CS retrievals make certain assumptions in the higher-latitude regions based upon the matchups between the TRMM PR and satellite observations in the Tropics. Some of these differences might also be addressed through improved representation within the databases (in both/either the XT and/or CS), or a more fundamental way the database is devised. For example,

databases are currently organized into bins of TPW and Ts (to be replaced by TPW and T2m in version 2), but since the XT sensors are less sensitive to the surface than the CS sensors due to their channel selection, the use of the Ts or T2m might be less useful or inappropriate for constraining the XT retrievals.

Both the observation-based CS-GPROF and model-based XT-GPROF schemes rely upon an *a priori* database for the physically-based precipitation retrieval within a Bayesian framework. However due to unique hybrid structure of traditional climate model and cloud-resolving models, the MMF provides more complete distributions of various types of precipitation and associated microwave Tb in sampling space. This approach is also beneficial for generating databases for various microwave instruments of GPM constellation partners, since it simply relies on the unified framework in terms of the cloud-precipitation model and the GPM forward model. On the other hand, retrieval errors and uncertainties depend on the quality of the MMF simulations and a forward model.

In the present study, the NASA MMF runs a 2D GCE with 4 km horizontal grid spacing and 41 vertical levels that is appropriate for resolving deep and organized convection. While it may not be suitable for numerically representing less-organized convection on a scale of less than 10-grid spacing of the GCE, the 4 km GCE horizontal grid spacing may effectively resolve cloud dynamics on the size of 40 km or larger. Even in the 3D grid framework with 1 km grid spacing, the GCE simulation does not necessarily represent the structure of isolated convection well (Matsui et al. 2009). For such intermediate-size convection, a grid size of at least 250 m is required for the realistic simulation of a precipitation system (Lang et al. 2014). The 2D grid

structure with homogeneous surface conditions also biases the updraft structure, cloud dynamics, and precipitation intensity and types in contrasting regions, such as between continental and ocean environments (Matsui et al. 2015). This may require heterogeneous surface patch (either land-cover types or land-ocean mask) in GCE to induce the necessary mesoscale pressure gradient to invigorate continental / island convection (Robinson et al. 2011). This sub-grid thermal patch may also create more realistic precipitation Tb signals on coastlines, where passive microwave retrievals typically have biases due to rapid gradient of the surface emissivity (Kidd 1998).

In future versions of the XT database, it is planned to relax these issues through conducting MMF simulations with finer-resolution GCE (250 m horizontal grid spacing) over sub-grid heterogeneous surface conditions. Importantly these new MMF simulations, with new physics and grid configurations, will be constrained against the GPM combined product (GPM-2BCMB), in terms of precipitation intensity, microphysics, and storm structure. In parallel, the MMF simulation will be evaluated against the GMI Tbs and DPR reflectivities statistics through the GPM simulator. Although the new MMF update could take significantly more computational time and effort, Matsui et al. (2015) established a convective- and microphysics quasi-equilibrium concept based on the time-invariant statistics of satellite observations over the entire Tropics. This concept suggests that single day statistics of microphysics and convection are similar to the climatology, as long as they are combined over the entire Tropics. This provides more rapid MMF development cycle; e.g., global statistics from single-day MMF simulation can be evaluated and constrained toward climatology statistics derived from the TRMM and GPM satellites.

Acknowledgements

Funding for this research is made possible through the NASA/University of Maryland master grant #526697/T613. The authors wish to thank NSSL and CEDA for the provision of the surface data sets, the GPM PPS team for provision of the satellite datasets.

Appendix. MMF-GPROF database improvement.

Figure A1a shows the improvement of the MMF-simulated microphysics characteristics of deep convective clouds (echo-top height > 7 km) in the forms of the TRMM Precipitation Radar (PR) Contoured Frequency of Altitude Diagram (CFAD). TRMM PR CFAD shows dramatic transition of reflectivity distributions. There are distinct three transitional zones: solid-phase zone (i.e., above 8km) where the presence of solid precipitation particles generated narrow and vertically constant reflectivity profiles, mixed-phase zone (i.e., between 5 and 8 km) where the aggregation and melting process of frozen particles dramatically increased reflectivity distributions, and liquid-phase zone (i.e., below 5 km) where liquid raindrops dominate the radar backscattering signals.

The CFAD from the MMF V1 database depart from characteristics of observed CFAD; e.g., maximum echo-top height is below 14km (lacking the undiluted hot tower), not distinct spectral broadening in the mixed-phase zone, underestimation of overall maximum echo signals throughout the profile due to lack of large precipitation particles. On the other hand, MMF V2 database show, yet not perfect, but the simulated CFAD structure has distinct three microphysics

zones and realistic distributions of solid/mixed/liquid-phase precipitation microphysics. Liquid-phase echo distributions are relatively overestimated ~5 dBZ. the improved (V2) MMF simulation provides, not yet perfect, but more realistic structure of the PR.

We also found that Gaussian weighting on the GCE column alignment are critical to formulate the Tb spectra for different sounder channels. Figure A1b shows the MHS-observed Tbs at 5 channels (89~190GHz) averaged for each instantaneous surface precipitation rate bin from TRMM PR 2A25 product; the Tbs become generally colder with more intense precipitation due to the effects of scattering. For light-precipitation (less than c. 2 mm h⁻¹) the 89 GHz channel shows a slight increase in Tb due to emission, thereafter decrease due to scattering. The higher frequencies show the 157 GHz and 190 GHz undergo the greatest scattering, followed by the 183±3GHz and 183±1GHz channels respectively. Importantly, at the 190GHz, 183±3GHz, and 183±1GHz channels, the associated thickness of the water vapor column results in the received signal being dominated by the elevated mixed- and solid-phase precipitation particles above lower troposphere; thus the scattering signal dominates the water vapor emission signal.

The original approach in simulating antenna-convolved Tb is to fold the 64×1 x-y 2D GCE grid into artificial 9×7 x-y grid, and then applying the Gaussian weighting (mimicking microwave antenna gain pattern) function to the center of 9×7 x-y grid. However, this method tends to misrepresent the Tb relationship among different sounder channels from light to heavy precipitation, in comparison with MHS-PR observations. Scattering magnitude for heavy rain generally converged into closer magnitude among different sounder channels, and top of that, scattering was significantly overestimated, and sampling of very heavy precipitation (> 15 mm hr⁻¹

¹) was completely lacked. When the Gaussian weighting function is applied directly to the 64x1 2D GCE grid, the sounder Tb relationship and scattering magnitude structure of all MHS channels was significantly improved toward observed patterns. This result physically infers that MMF-GPROF database requires realistic “structure” of cloud-precipitation-water vapor profiles.

References

Aires, F., C. Prigent, F. Bernardo, C. Jiménez, R. Saunders, P. Brunel, 2011: A Tool to Estimate Land-Surface Emissivities at Microwave frequencies (TELSEM) for use in numerical weather prediction, *Quart. J. Roy. Meteor. Soc.*, **137**, 690–699.

Berg, W, T. L’Ecuyer, and C. Kummerow, 2006: Rainfall Climate Regimes: The relationship of regional TRMM rainfall biases in the environment. *J. Appl. Meteor. Climatol.* **45**, 434-454.

Boukabara, S-A., K. Garrett, W. Chen, F. Iturbide-Sanchez, C. Grassotti, C. Kongoli, R. Y. Chen, Q. H. Liu, B. H. Yan, F. Z. Weng, R. Ferraro, T. J. Kleespies and H. Meng, 2011: MiRS: An All-Weather 1DVAR Satellite Data Assimilation and Retrieval System, *IEEE Trans. Geosci. Remote Sens.*, **49**, 3249-3272

Casella, D., G. Panegrossi, P. Sano, L. Milani, M. Petracca and S. Dietrich, 2015: A novel algorithm for detection of precipitation in tropical regions using PMW radiometers. *Atmos. Meas. Tech.* **8**, 1217-1232

Chern, J.-D., W.-K. Tao, S. E. Lang, J.-L. F. Li, K. I. Mohr, G. S. Jackson, and C. D. Peters-Lidard, 2015: Performance of the Goddard Multi-scale Modeling Framework with Goddard microphysical schemes. Submitted to *J. Adv. Model. Earth Syst.*

689 Ebert, E. E., J. E. Janowiak, and C. Kidd, 2007: Comparison of Near Real Time Precipitation
 690 Estimates from Satellite Observations and Numerical Models. *Bull. Amer. Meteor. Soc.* **88**, 47-
 691 64
 692 Elsaesser, GS and C. D. Kummerow, 2015: The Sensitivity of Rainfall Estimation to Error
 693 Assumptions in a Bayesian Passive Microwave Retrieval Algorithm. *J. Appl. Meteor. Climatol.*
 694 **54**, 408-422 doi: 10.1175/JAMC-D-14-0105.1
 695 Ferraro, R. R., E. A. Smith, W. Berg, and G. J. Huffman, 1998: A screening methodology for
 696 passive microwave precipitation retrieval algorithms. *J. Atmos. Sci.*, **55**, 1583-1600
 697 Hou, A. Y., R. K. Kakar, S. Neeck, A. A. Azarbarzin, C. D., Kummerow, M. Kojima, R. Oki, K.
 698 Nakamura, and T. Iguchi, 2014: The Global Precipitation Measurement Mission. *Bull. Amer.*
 699 *Meteor. Soc.* **5**, 701-722. doi=10.1175/BAMS-D-13-00164.1
 700 Iturbide-Sanchez, F., S-A. Boukabara, R. Chen, K. Garrett, C. Grassotti, W. Chen and F. Weng,
 701 2011: Assessment of a variational inversion system for rainfall rate over land and water surfaces.
 702 *IEEE Trans. Geosci. Remote Sens.* 49, 3311-3333
 703 Kidd, C., 1998: On rainfall retrieval using polarization-corrected temperatures. *Int. J. Remote*
 704 *Sens.*, **19**, 981–996.
 705 Kidd, C., D. Kniveton, and E.C. Barrett, 1998: Advantage and disadvantages of
 706 statistical/empirical satellite estimation of rainfall. *J. Atmos. Sci.* **55**, 1576-1582.
 707 Kidd, C. and G. Huffman, 2011: Global Precipitation Measurement. *Meteor. App.* **18**, 334-353.
 708 doi: 10.1002/met.284
 709 Kidd, C. and V. Levizzani, 2011: Satellite precipitation retrievals. *Hydrol. Earth Syst. Sci.*
 710 *Discus.* **7**, 8157-8177. doi:10.5194/hessd-8-8157-2010

711 Kidd, C., P. Bauer, J. Turk, G. J. Huffman, R. Joyce, K-L. Hsu, and D. Braithwaite, 2012: Inter-
 712 comparison of high-resolution precipitation products over northwest Europe. *J. Hydrometeor.*
 713 13, 67-83. doi: 10.1175/JHM-D-11-042

714 Kidd, C. and A. Hou, 2012: Combined satellite-surface precipitation products: assessment of
 715 regional and temporal characteristics and relationships. EGU General Assembly Conference
 716 Abstracts 14, p.3459. European Geophysical Union, Vienna, Austria, 22-27 April 2012.

717 Kidd, C. 2014a: last updated 2014: GPROF NOAA-18 MHS Level 2A precipitation product.
 718 NASA/GSFC, Greenbelt, MD, USA. doi=10.5067/GPM/MHS/NOAA18/GPROF2A

719 Kidd, C. 2014b: last updated 2014: GPROF NOAA-19 MHS Level 2A precipitation product.
 720 NASA/GSFC, Greenbelt, MD, USA. doi=10.5067/GPM/MHS/NOAA19/GPROF2A

721 Kidd, C. 2014c: last updated 2014: GPROF EUMETSAT MetOpA MHS Level 2A precipitation
 722 product. NASA/GSFC, Greenbelt, MD, USA. doi=10.5067/GPM/MHS/METOPA/GPROF2A

723 Kidd, C. 2014d: last updated 2014: GPROF EUMETSAT MetOpB MHS Level 2A precipitation
 724 product. NASA/GSFC, Greenbelt, MD, USA. doi=10.5067/GPM/MHS/METOPB/GPROF2A

725 Kirstetter, P. E., Y. Hong, J. J. Gourley, S. Chen, Z. Flamig, J. Zhang, M. Schwaller, W. Petersen
 726 and E. Amitai, 2012: Toward a Framework for Systematic Error Modeling of Spaceborne
 727 Precipitation Radar with NOAA/NSSL Ground Radar-based National Mosaic QPE. *J.*
 728 *Hydrometeor.*, 13, 4, 1285-1300. doi:10.1175/JHM-D-11-0139.1

729 Kummerow, C., 1993: On the accuracy of the Eddington approximation for radiative transfer in
 730 the microwave frequencies. *J. Geophys. Res.*, **98**, 2757-2765.

731 Kummerow, C.D. and L. Giglio, 1994: A Passive Microwave Technique for Estimating Rainfall
732 and Vertical Structure Information from Space. Part I: Algorithm Description. *J. Appl. Meteor.*,
733 **33**, 3–18.

734 Kummerow, C., W. S. Olson and L. Giglio, 1996: A simplified scheme for obtaining
735 precipitation and vertical hydrometeor profiles from passive microwave sensors. *IEEE Trans.*
736 *Geosci. Remote Sens.*, **34**, 1213-1232.

737 Kummerow, C., Y. Hong, W. S. Olson, S. Yang, R. F. Alder, J. McCollum, R. Ferraro, G. Petty,
738 D-B. Shin, and T. T. Wilheit, 2001: The evolution of the Goddard profiling algorithm (GPROF)
739 for rainfall estimation from passive microwave sensors. *J. Appl. Meteor.*, **40**, 1801-1820.

740 Kummerow, C. 2014a: last updated 2014: GPROF GCOMW1 AMSR2 Level 2A precipitation
741 product. NASA/GSFC, Greenbelt, MD, USA. doi=10.5067/GPM/AMSR/GCOMW1/GPROF2A

742 Kummerow, C. 2014b: last updated 2014: GPROF GPM GMI Level 2A precipitation product.
743 NASA/GSFC, Greenbelt, MD, USA. doi=10.5067/GPM/GMI/GPM/GPROF2A

744 Kummerow, C. 2014c: last updated 2014: GPROF DMSP-F16 SSMIS Level 2A precipitation
745 product. NASA/GSFC, Greenbelt, MD, USA. doi=10.5067/GPM/SSMIS/F16/GPROF2A

746 Kummerow, C. 2014d: last updated 2014: GPROF DMSP-F17 SSMIS Level 2A precipitation
747 product. NASA/GSFC, Greenbelt, MD, USA. doi=10.5067/GPM/SSMIS/F17/GPROF2A

748 Kummerow, C. 2014e: last updated 2014: GPROF DMSP-F18 SSMIS Level 2A precipitation
749 product. NASA/GSFC, Greenbelt, MD, USA. doi=10.5067/GPM/SSMIS/F18/GPROF2A

750 Kummerow, C., D. L. Randel, M. Kulie, N-Y. Wang, R. Ferraro, S. J. Munchak and V. Petkovic
751 2015: The evolution of the Goddard PROFiling algorithm to a fully parametric scheme.
752 Submitted to Journal of Atmospheric and Oceanic Technology.

753 Lang, S., W.-K. Tao, J.-D. Chern, D. Wu, and X. Li, 2014: Benefits of a 4th ice class in the
 754 simulated radar reflectivities of convective systems using a bulk microphysics scheme. *J.*
 755 *Atmos. Sci.* (in press) doi: 10.1175/JAS-D-13-0330.1

756 Laviola, S., V. Levizzani, E. Cattani, and C. Kidd, 2013: The 183-WSL fast rain rate retrieval
 757 algorithm. Part II: Validation using ground radar measurements. *Atmos. Res.* **134**, 77-86.

758 Matsui, T., X. Zeng, W.-K. Tao, H. Masunaga, W. Olson, and S. Lang, 2009: Evaluation of long-
 759 term cloud-resolving model simulations using satellite radiance observations and multifrequency
 760 satellite simulators. *J. Atmos. Oceanic Technol.*, **26**, 1261-1274.

761 Matsui, T., T. Iguchi, X. Li, M. Han, W.-K. Tao, W. Petersen, T. L'Ecuyer, R. Meneghini, W.
 762 Olson, C. D. Kummerow, A. Y. Hou, M. R. Schwaller, E. F. Stocker, J. Kwiatkowski (2013),
 763 GPM satellite simulator over ground validation sites, *Bull. Amer. Meteor. Soc.*, **94**, 1653–1660.
 764 doi: 10.1175/BAMS-D-12-00160.1

765 Matsui, T., W.-K. Tao, S. J. Munchack, G. Huffman, and M. Grecu, 2015: Satellite View of
 766 Quasi-Equilibrium States in Tropical Convection and Precipitation Microphysics, *Geophys. Res.*
 767 *Lett.*, **42**, doi:10.1002/2015GL063261

768 Met Office, 2003: Met Office Rain Radar Data from the NIMROD System. NCAS British
 769 Atmospheric Data Centre, accessed 9 April 2015.
 770 <http://catalogue.ceda.ac.uk/uuid/82adec1f896af6169112d09cc1174499>

771 Mohr, K. I., W.-K. Tao, J.-D. Chern, S. V. Kumar, and C. Peters-Lidard, 2012: The NASA-
 772 Goddard Multi-scale Modeling Framework-Land Information System: Global land/atmosphere
 773 interaction with resolved convection. *Environmental Modeling and Software*, **39**, 103-115.

774 Olson, W. S., P. Bauer, C. D. Kummerow, Y. Hong, W.-K. Tao, 2001: A melting-layer model
775 for passive/active microwave remote sensing applications. Part II: simulation of TRMM
776 observations. *J. Appl. Meteorol.*, **40**, 1164–1179.

777 Olson, W., S. S. Yang, J. E. Stout and M. Grecu, 2007: The Goddard Profiling Algorithm
778 (GPROF): description and current applications, in Measuring Precipitation from Space:
779 EURAINSAT and the future. Eds. Levizzani, V; Bauer, P; Turk, FJ, *Adv. Global Change Res.*
780 **28**, 179

781 Robinson, F. J., S. C. Sherwood, D. Gerstle, C. Liu, and D. J. Kirshbaum, 2011: Exploring the
782 Land–Ocean Contrast in Convective Vigor Using Islands. *J. Atmos. Sci.*, **68**, 602–618. doi:
783 10.1175/2010JAS3558.1

784 Sano, P., G. Panegrossi, D. Casella, F. Di Paola, L. Milani, A. Mugnai, M. Petracca and S.
785 Dietrich, 2015: The Passive microwave Neural network Precipitation Retrieval (PNPR)
786 algorithm for AMSU/MHS observations: description and application to European case studies.
787 *Atmos. Meas. Tech.* 8, 837-857. doi: 10.5194/amt-8-837-2015

788 Smith, E. A., C. Kummerow and A. Mugnai, 1994: The emergence of inversion-type profile
789 algorithm for estimation of precipitation from satellite passive microwave measurements.
790 *Remote Sens. Reviews*, **11**, 211-242.

791 Spencer, R. W. 1986: A satellite passive 37 GHz scattering-based method for measuring oceanic
792 rain rates. *J. Climate and App. Meteor.* **25**, 754-766.

793 Surussavadee, C., D. H. Staelin, 2008: Global Millimeter-Wave Precipitation Retrievals Trained
794 With a Cloud-Resolving Numerical Weather Prediction Model, Part 1: Retrieval Design. *IEEE*
795 *Trans. Geosci. Remote Sens.* 46, 99-108.

796 Tao, W.-K. and J. Simpson 1993: Goddard Cumulus Ensemble Model. Part 1: Model
797 description. *Terr. Atmos. Oceanic Sci.*, **4**, 35-72.

798 Tao, W.-K., J.-D. Chern, R. Atlas, D. Randall, X. Lin, M. Khairoutdinov, J.-L. Li, D. E. Waliser,
799 A. Hou, C. Peters-Lidard, W. Lau, and J. Simpson, 2009: A Multi-scale modeling
800 system: Development, applications and critical issues. *Bull. Amer. Meteor. Soc.*, **90**, 515-534

801 Tripoli, G. J. 1992: A non-hydrostatic model designed to simulate scale interaction. *Mon. Wea.*
802 *Rev.*, **120**, 1342-1359.

803 Webb, M., C. Senior, S. Bony, J. J. Morcrette, 2001: Combining ERBE and ISCCP data to assess
804 clouds in the Hadley Centre, ECMWF and LMD atmospheric climate models, *Climate*
805 *Dynamics*, **17**, 905-922. doi: 10.1007/s003820100157

806 Wilheit, T. T., 1979: A model for the microwave emissivity of the ocean's surface as a function
807 of wind speed. *IEEE Trans. Geosci. Electron.*, **GE-17**, 244-249.

808

809

Captions:

Table 1: Sensors contributing to the Global Precipitation Measurement mission constellation together with the scan type and frequencies used (those in italics are not included in this study).

Table 2: Representation of occurrence (%) of light rainfall and ratio of accumulation for comparison over the United States.

Figure 1: Generic processing steps for the GPROF retrieval scheme

Figure 2: Mean rain rate per GPROF database bin for GMI (left) and MHS (right). Units for g Kg^{-1} for TPW and K for Ts.

Figure 3: Ratio of rainfall accumulation by rain intensity over the United States for the AMSR2, GMI, MHS and SSMIS retrievals.

Figure 4: Rain/no-rain threshold for GPROF satellite retrievals based upon comparison of MRMS surface radar rainfall vs satellite rainfall estimates. A surface radar quality index of 1.0 (best quality) was used; period of study 6 March 2014 - 5 March 2015

Figure 5. Distribution of daily correlation coefficients (upper plot) and RMSE (lower plot) over the United States based upon instantaneous precipitation retrievals from the AMSR2, GMI, MHS and SSMIS sensors at the sensor resolution. The clear outlined bars (upper plot) and dashed line (lower plot) represent the performance of the SSMIS retrievals at 15 x 15 km resolution rather

than the 44.2 x 27.5 km retrieval resolution. Only days with an occurrence of precipitation > 1% are included in the comparison.

Figure 6. Distribution of daily correlation coefficients (upper plot) and RMSE (lower plot) over Western Europe based upon instantaneous precipitation retrievals from the AMSR2, GMI, MHS and SSMIS sensors at the sensor resolution. The clear outlined bars (upper plot) and dashed line (lower plot) represent the performance of the SSMIS retrievals at 15 x 15 km resolution rather than the 44.2 x 27.5 km retrieval resolution. Only days with an occurrence of precipitation > 1% are included in the comparison.

Figure 7. Occurrence of daily-scale correlation coefficients for MHS retrievals over the US for nadir (23-68) and edge-of-scan (1-22 and 69-90) scan positions.

Figure 8: Maps of correlation coefficients generated from instantaneous satellite/surface matchups for the period 6 March 2014 through 5 March 2015 on a $1^\circ \times 1^\circ$ grid at the native retrieval resolution of the satellite estimates (*a-d*) and for the SSMIS at 15×15 km resolution (*e*).

Figure 9: Global maps of annual precipitation covering the period 6 March 2014 through 5 March 2015 for AMSR2, GMI, MHS and SSMIS.

Figure 10: Plots of the percent occurrence of rain intensities for instantaneous retrievals for three latitudinal groups, high latitudes (90° - 60°), mid-latitudes (30° - 60°) and the Tropics (30° - 30°), for land and ocean.

Figure 11: Latitudinal profiles of mean daily rainfall (mm d^{-1}) for 6 March 2014 through 5 March 2015.

Figure A1: a) Contoured Frequency of Altitude Diagram (CFAD) of deep convection (echo-top height > 7 km) for TRMM PR and MMF V1 and MMF V2 database; b) Tb-rainrate plot from MHS-TRMM PR co-temporal/co-located data (*left*), and data simulated from MMF with different Gaussian weighting with either 9×7 grid (*center*) or 64×1 (*right*) grid configuration.

867 Table 1: Sensors contributing to the Global Precipitation Measurement mission constellation
868 together with the scan type and frequencies used (those in italics are not included in this study).

Sensor	SSMIS	AMSR2	<i>TMI</i>	GMI	MHS	<i>SAPHIR</i>	<i>ATMS</i>
Satellite	DMSP-F16, F17, F18, <i>F19</i>	GCOMW1	<i>TRMM</i>	GPM	NOAA18,19, MetOp-A, B	<i>Megha- Tropiques</i>	<i>NPP</i>
Scan type	Conical	Conical	<i>Conical</i>	Conical	Cross-track	<i>Cross-track</i>	<i>Cross-track</i>
frequencies	19.35VH 22.235V 37.0VH 50.3-63.3VH 91.65VH 150H 183.31H	6.925/7.3VH 10.65VH 18.70VH 23.80VH 36.5VH 89.0VH	<i>10.65VH</i> <i>18.70VH</i> <i>23.80VH</i> <i>36.5VH</i> <i>89.0VH</i>	10.65VH 18.70VH 23.80V 36.5VH 89.0VH 165.6VH 183.31V(2)	89V 157V 183.31H (2) 190.31V	<i>183.31H(6)</i>	23.8 31.4 50-3-57.3 87-91 164-167 183.31(5)
Samples/ scan	180	486	208	221	90	182	96
FOV* (Nadir/37 GHz)	44.2 x 27.5 km	12 x 7 km	<i>16 x 9 km</i>	14 x 8.6 km	15.88 x15.88 km	<i>10 x 10 km</i>	<i>16 x 16 km</i>
Sampling *	12.5 x 12.5 km	10 x 7 km	<i>13.7 x 6 km</i>	13.4 x 8 km	15.88 km x variable	<i>10 km x variable</i>	<i>16 km x variable</i>

869 * Figures are for along-track x cross-track dimensions.

870

871 Table 2: Summary of key characteristics of the CS-GPROF and XT-GPROF schemes

872

Feature	CS-GPROF	XT-GPROF
Database	Observation-based	MMF model-based
Surface types	15 categories	Surface-blind
Resolution	37 GHz channel*	15.88 x 15.88 km (MHS)
TPW range	0-80 g Kg ⁻¹	0-95 g Kg ⁻¹
Ts range	230-337 K	189-344 K
Snow retrieval	Diagnostic	Retrieval

873 *SSMIS = 44.2 x 27.5 km; AMSR2 = 12 x 7 km; GMI = 14 x 8.6 km.

874

875

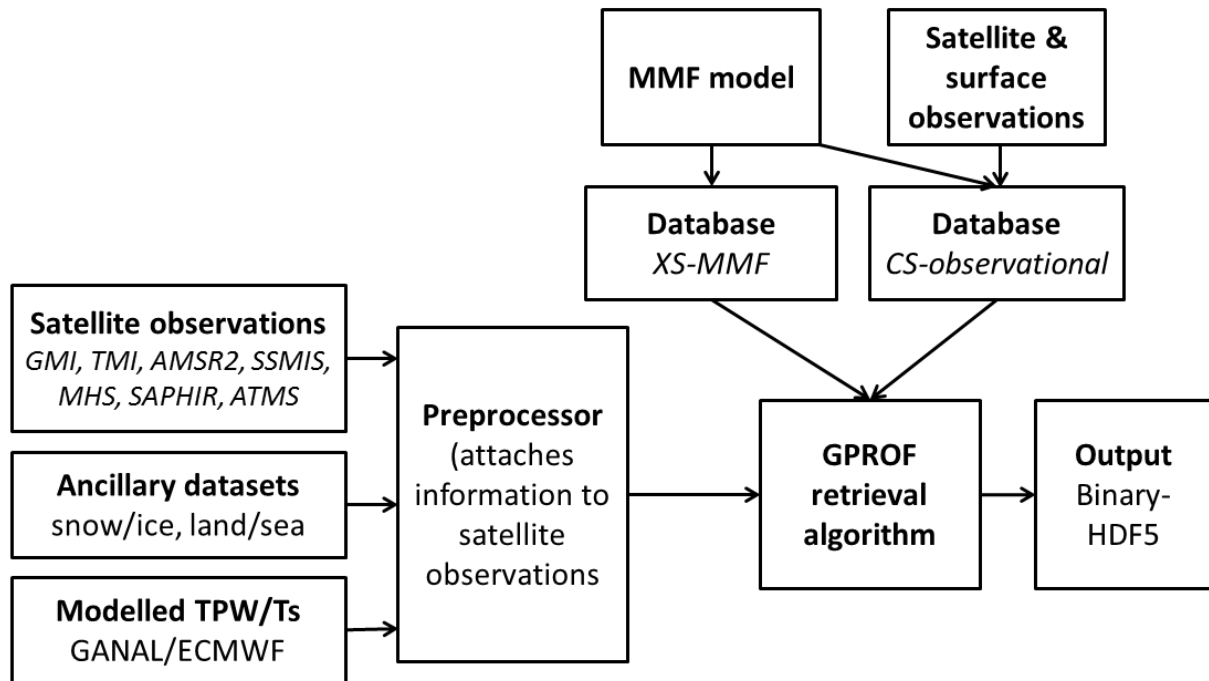
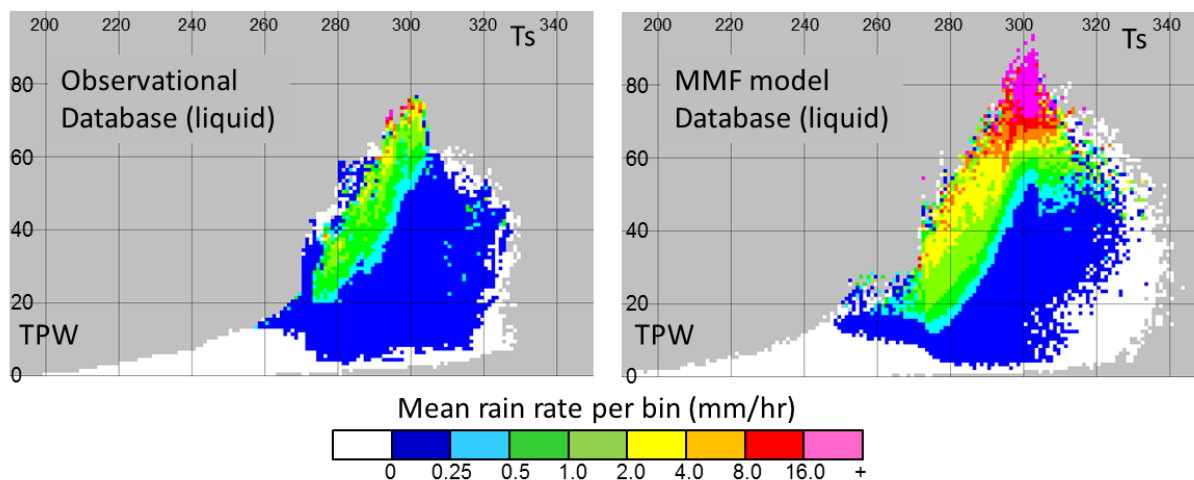


Figure 1: Generic processing steps for the GPROF retrieval scheme

880



881

882 Figure 2: Mean rain rate per GPROF database bin for GMI (left) and MHS (right). Units are g

883 Kg⁻¹ for TPW and K for Ts.

884

885

886

887

888

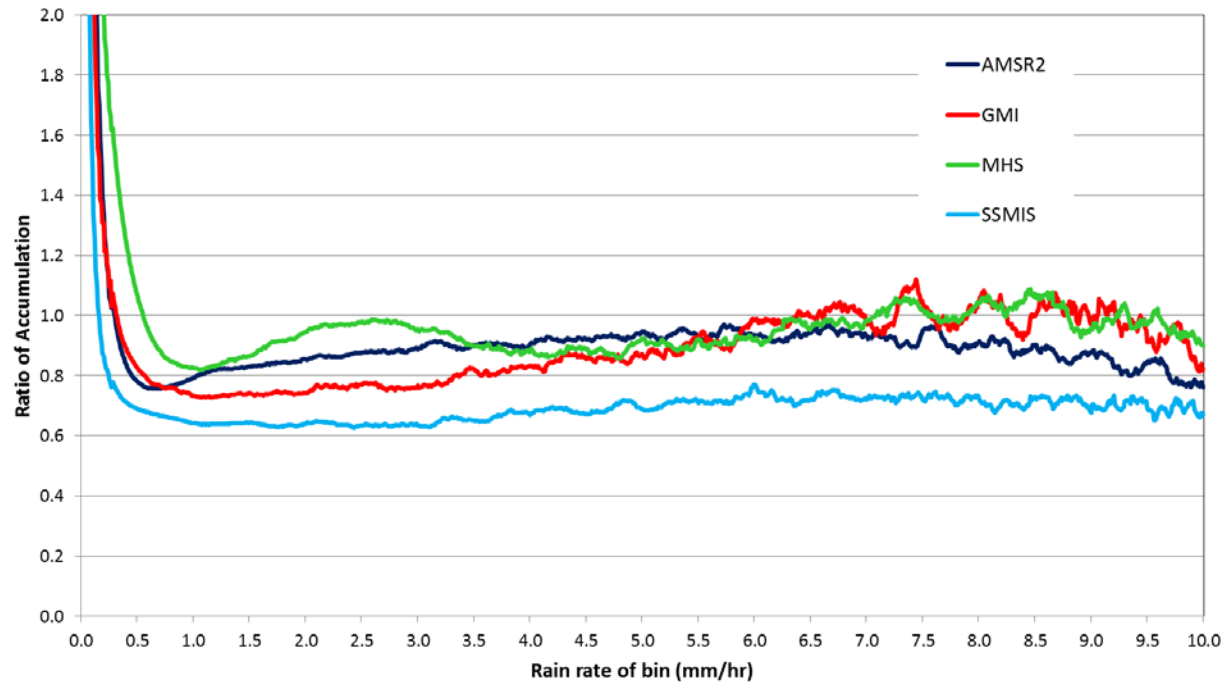
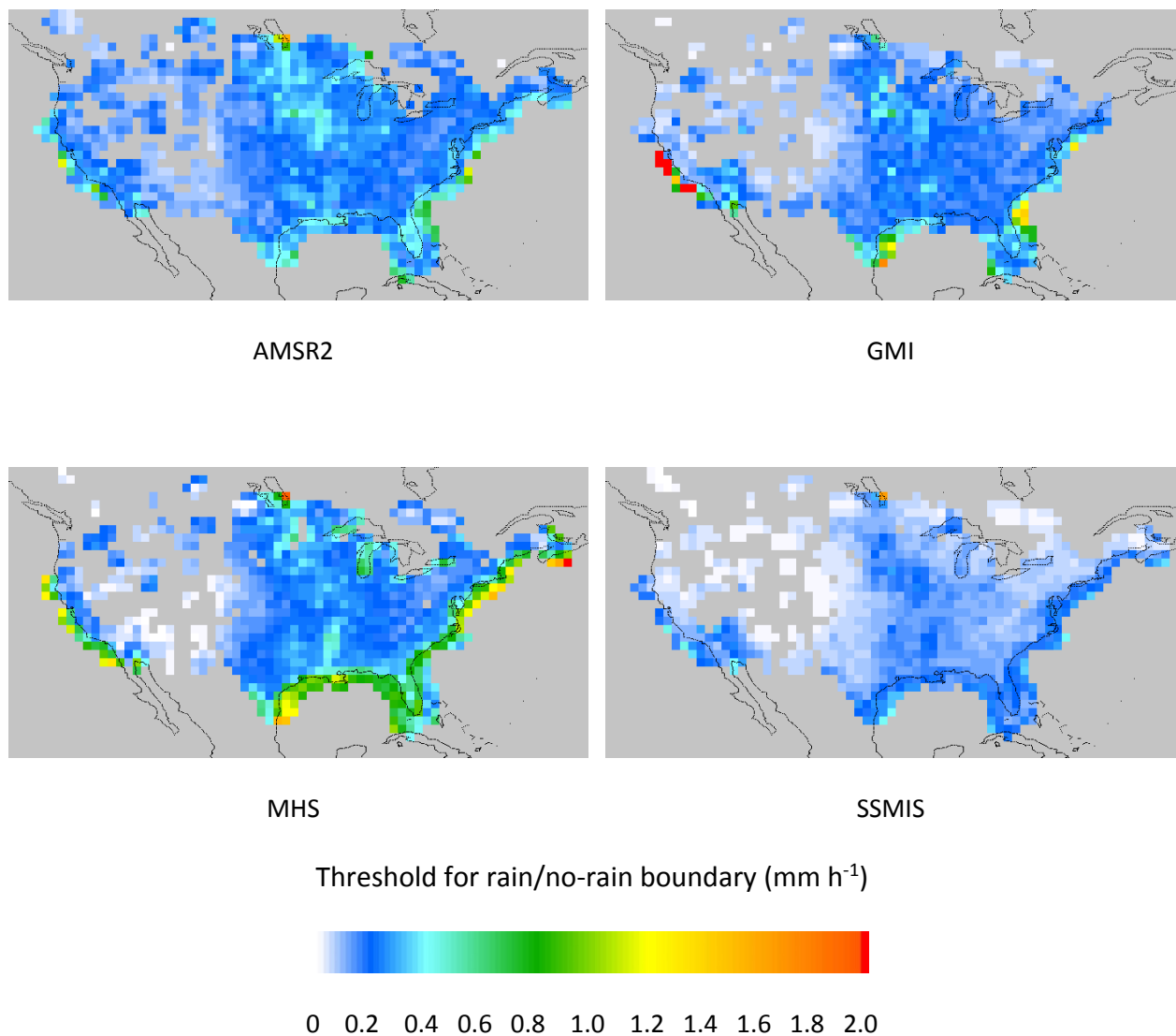


Figure 3: Ratio of rainfall accumulation by 0.01 mm h⁻¹ rain intensity bin over the United States for the AMSR2, GMI, MHS and SSMIS retrievals.

894



895

896

897

898

899 Figure 4: Rain/no-rain thresholds for GPROF satellite retrievals based upon matched
900 satellite/surface radar occurrences of precipitation for the study period from 6 March 2014 to 5
901 March 2015.

902

903

904

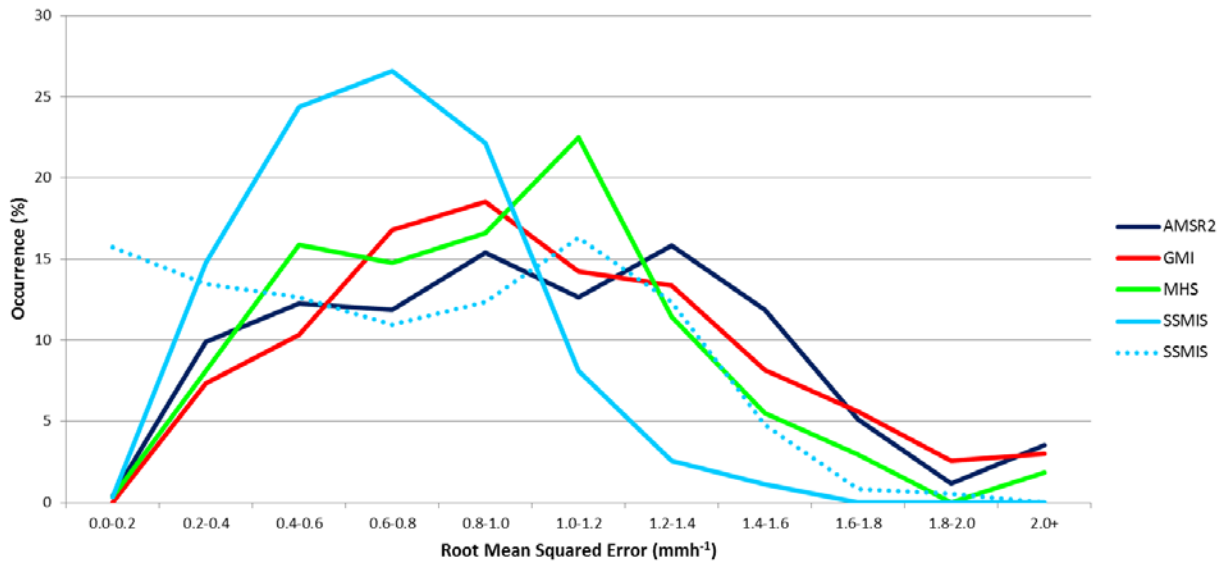
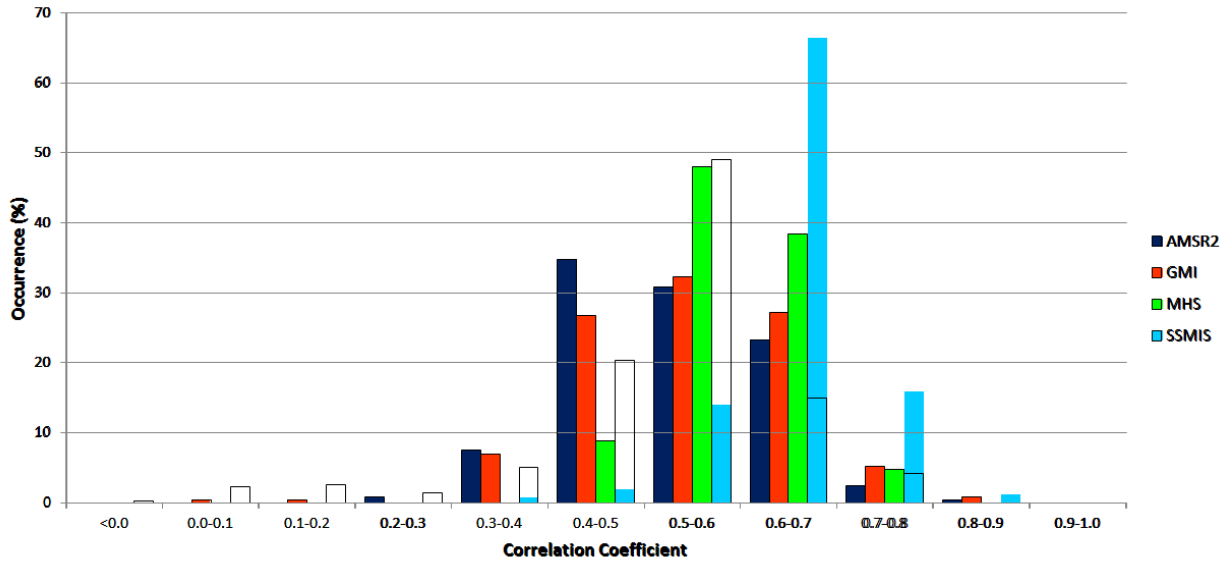


Figure 5. Distribution of daily correlation coefficients (upper plot) and RMSE (lower plot) over the United States based upon instantaneous precipitation retrievals from the AMSR2, GMI, MHS and SSMIS sensors at the sensor resolution. The clear outlined bars (upper plot) and dashed line (lower plot) represent the performance of the SSMIS retrievals at 15 x 15 km resolution rather than the 44.2 x 27.5 km retrieval resolution. Only days with an occurrence of precipitation > 1% are included in the comparison.

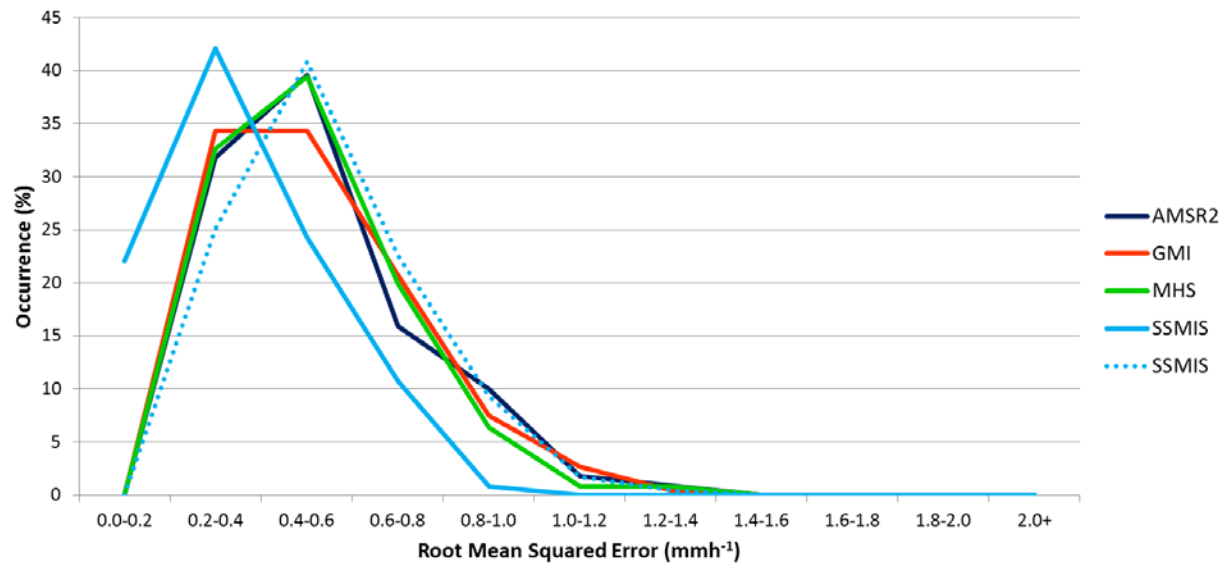
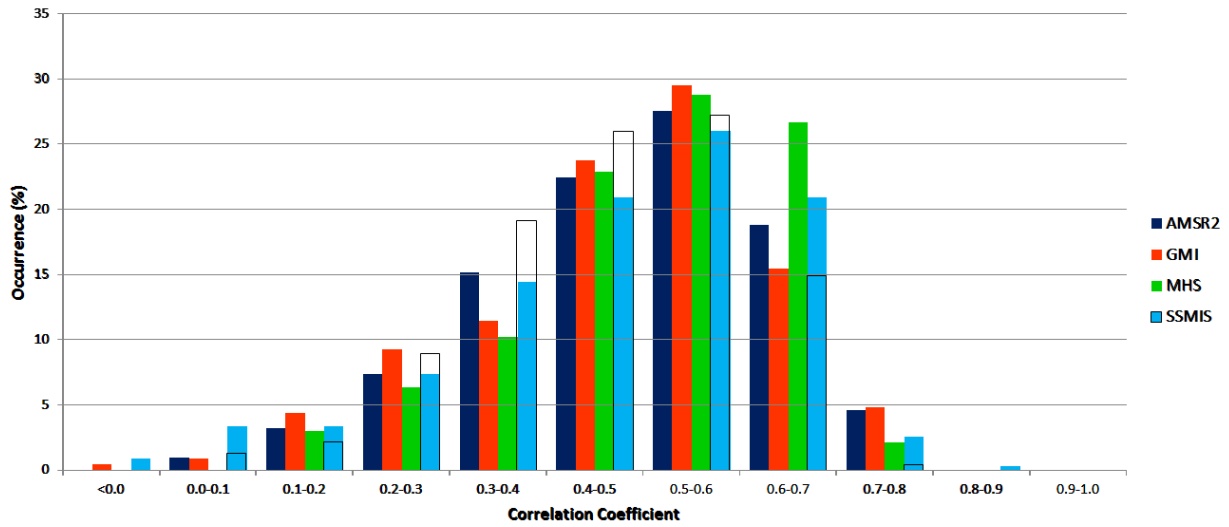


Figure 6. Distribution of daily correlation coefficients (upper plot) and RMSE (lower plot) over Western Europe based upon instantaneous precipitation retrievals from the AMSR2, GMI, MHS and SSMIS sensors at the sensor resolution. The clear outlined bars (upper plot) and dashed line (lower plot) represent the performance of the SSMIS retrievals at 15 x 15 km resolution rather than the 44.2 x 27.5 km retrieval resolution. Only days with an occurrence of precipitation > 1% are included in the comparison.

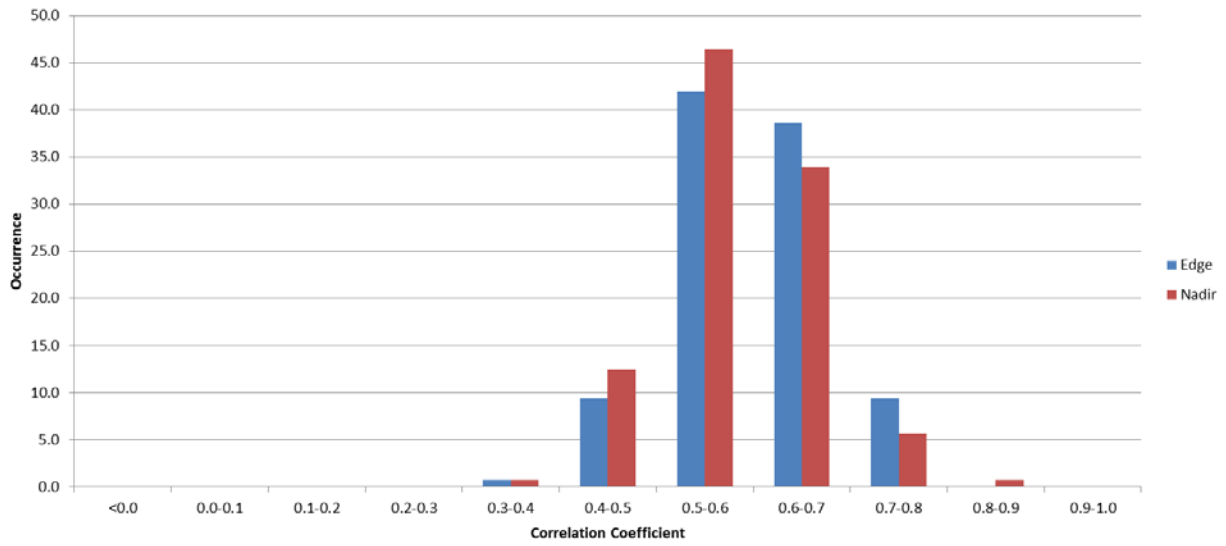
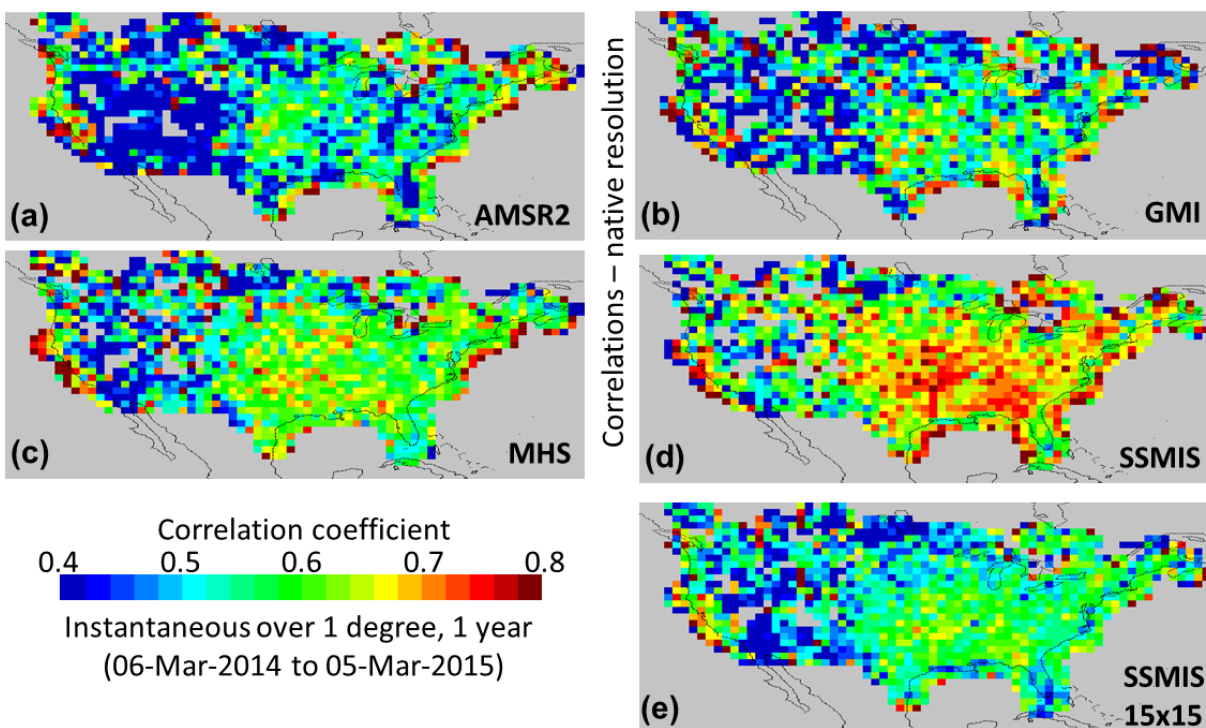


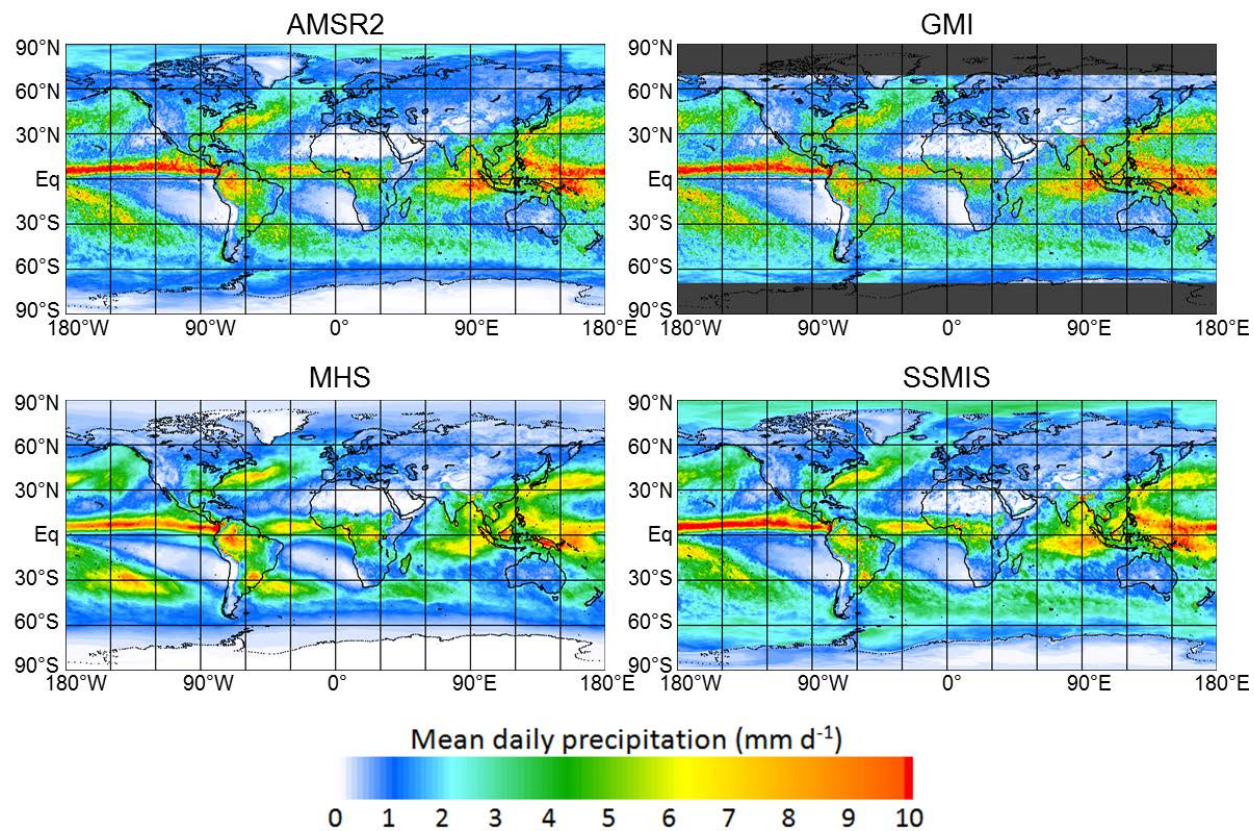
Figure 7. Occurrence of daily-scale correlation coefficients for MHS retrievals over the US for nadir (23-68) and edge-of-scan (1-22 and 69-90) scan positions.



929

930 Figure 8: Maps of correlation coefficients generated from instantaneous satellite/surface
 931 matchups for the period 6 March 2014 through 5 March 2015 on a $1^\circ \times 1^\circ$ grid at the native
 932 retrieval resolution of the satellite estimates (*a-d*) and for the SSMIS at 15×15 km resolution
 933 (*e*).

934



935

936 Figure 9: Global maps of mean daily precipitation covering the period 6 March 2014 through 5

937 March 2015 for AMSR2, GMI, MHS and SSMIS.

938

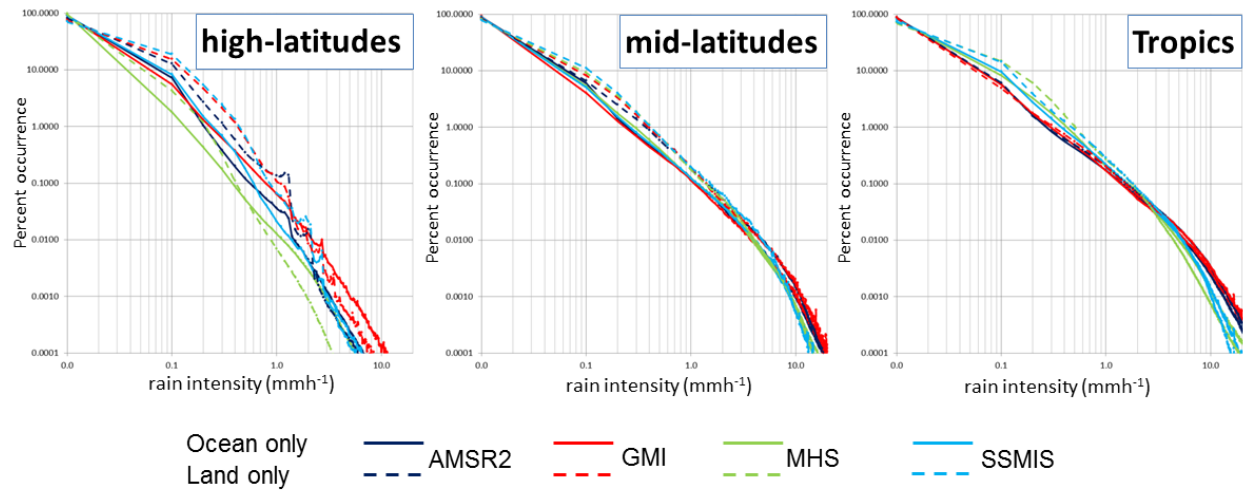
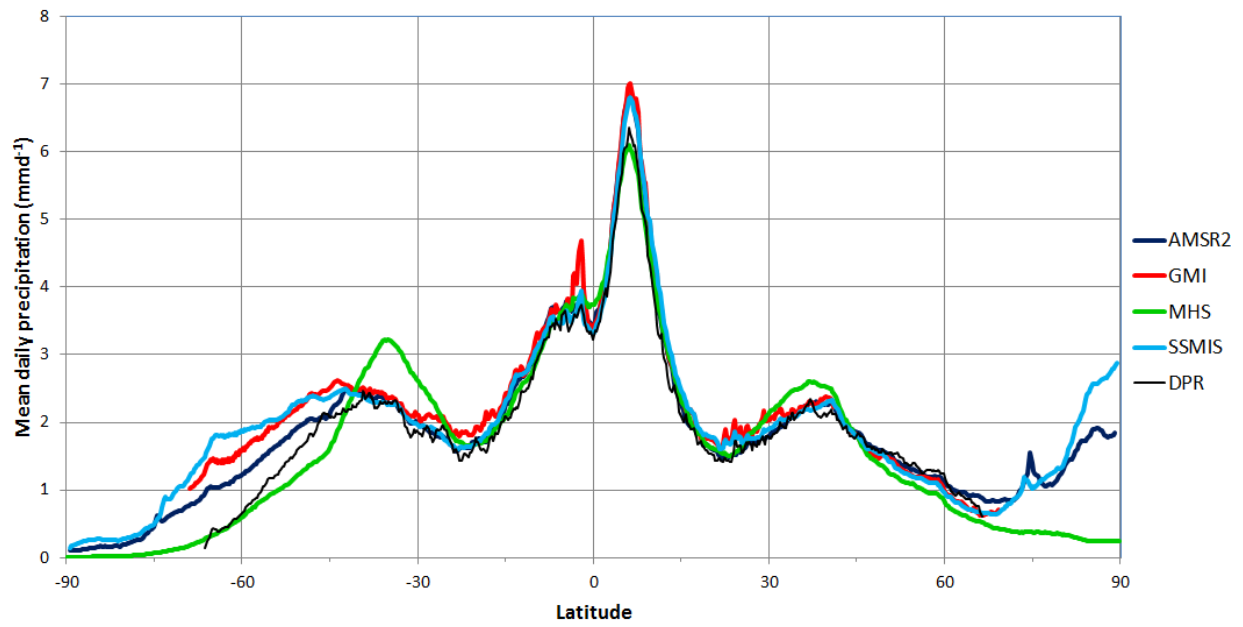


Figure 10: Plots of the percent occurrence of rain intensities for instantaneous retrievals for three latitudinal groups, high latitudes (90° - 60°), mid-latitudes (30° - 60°) and the Tropics (30° - 30°), for land and ocean.

944



945

946 Figure 11: Latitudinal profiles of mean daily precipitation for 6 March 2014 through 5 March
947 2015.

948

949

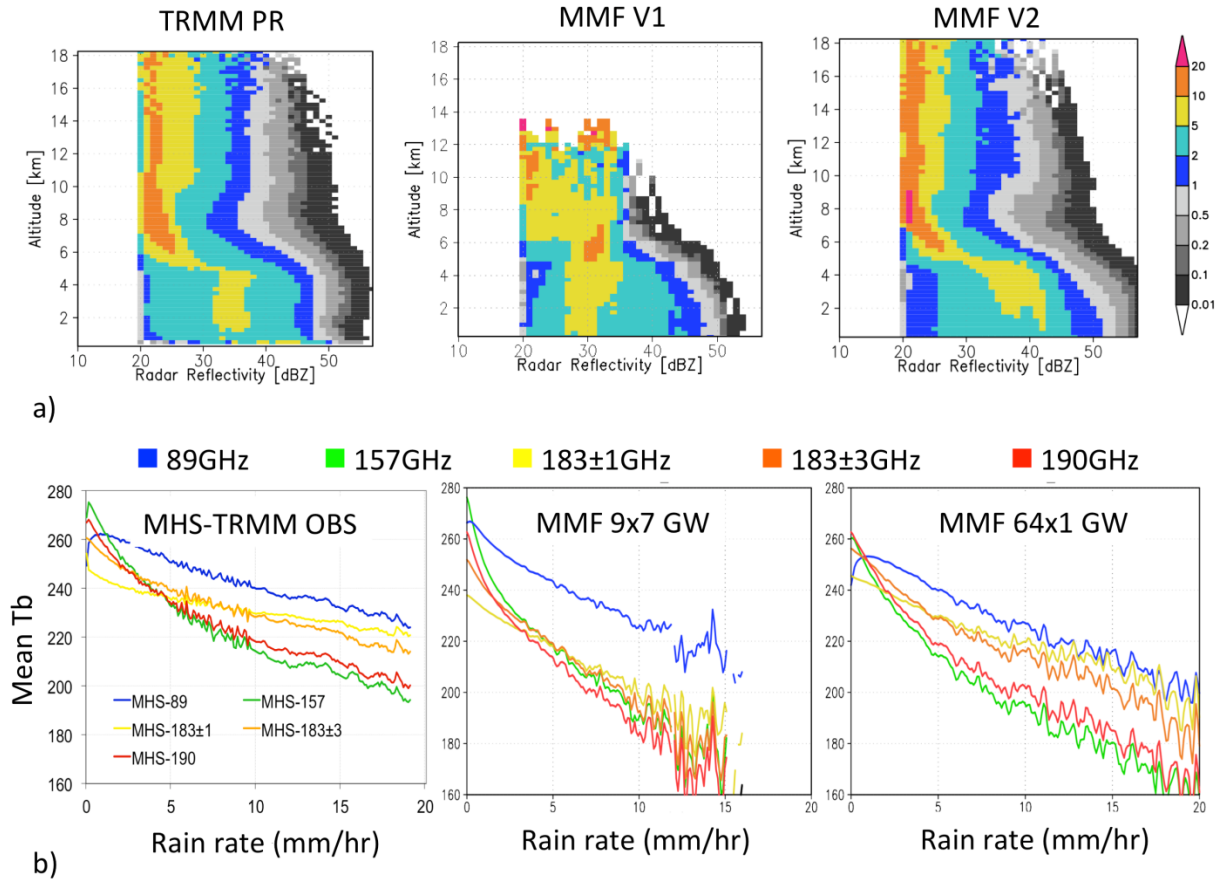


Figure A1: a) Contoured Frequency of Altitude Diagram (CFAD) of deep convection (echo-top height > 7 km) for TRMM PR and MMF V1 and MMF V2 database; b) Tb-rainrate plot from MHS-TRMM PR co-temporal/co-located data (*left*), and data simulated from MMF with different Gaussian weighting with either 9x7 grid (*center*) or 64x1 (*right*) grid configuration.